J. Fluid Mech. (1990), *vol.* 210, *pp.* 1–21
Printed in Great Britain

The instability of a moving viscous drop

By C. POZRIKIDIS

Department of Applied Mechanics and Engineering Sciences, R-011,
University of California at San Diego, La Jolla, CA 92093, USA

(Received 18 November 1988 and in revised form 3 February 1989)

The deformation of a moving spherical viscous drop subject to axisymmetric perturbations is considered. The problem is formulated using two different variations of the boundary integral method for Stokes flow, one due to Rallison & Acrivos, and the other based on an interfacial distribution of Stokeslets. An iterative method for solving the resulting Fredholm integral equations of the second kind is developed, and is implemented for the case of axisymmetric motion. It is shown that in the absence of surface tension, a moving spherical drop is unstable. Prolate perturbations cause the ejection of a tail from the rear of the drop, and the entrainment of a thin filament of ambient fluid into the drop. Oblate perturbations cause the drop to develop into a nearly steady ring. The viscosity ratio plays an important role in determining the timescale and the detailed pattern of deformation. Filamentation of the drop emerges as a persistent but secondary mechanism of evolution for both prolate and oblate perturbations. Surface tension is not capable of suppressing the growth of perturbations of sufficiently large amplitude, but is capable of preventing filamentation.

1. Introduction

The structure and dynamics of viscous drops has received considerable attention in recent years (Harper 1972; Clift, Grace & Weber 1978; Rallison 1984; Zinemanas & Nir 1988). Interest in the subject is primarily motivated by the need to understand the rheology of emulsions, to delineate the mechanics of heterogeneous mixing, and to analyse the deformation of biological cells. Additional impetus for research has been provided by the observation that aggregates of microscopic particles and microorganisms show behaviour similar to that of suspended homogeneous viscous drops (Kojima, Hinch & Acrivos 1984). This renders the drops convenient prototypes for studying the formation or destruction of structure in dispersed systems.

One of the most important problems within the general area of drop mechanics concerns the shape of drops moving under the action of gravity. Hadamard and Rybczynski showed that at zero Reynolds number, the flow associated with the spherical shape satisfies all of the necessary boundary conditions for steady motion independently of surface tension (Batchelor 1967, p. 235). Extending these results, Kojima *et al.* (1984) showed that steady drops with a slightly spherical simply connected shape may not exist, suggesting that moving drops are either spherical or highly deformed. Since there appears to be no theoretical or experimental evidence for steadily moving highly deformed drops, it appears that the spherical shape is the only possible steady configuration. Before the spherical drop can be accepted as a physically viable configuration however, the stability of its motion must be assessed.

Important information on the stability of a moving viscous drop was recently provided by Kojima *et al.* (1984). These authors observed the behaviour of a heavy drop falling into a pool of a lighter, miscible fluid, and reported a sequence of stages in the drop evolution. In the first stage, soon after entrance, the drop developed an elongated tail; in the second stage, the tail separated from the main body of the drop, and the drop flattened and developed an intrusion at the rear stagnation point; in the third stage, the intrusion grew in size, producing an axisymmetric, expanding drop ring; in the last stage, the ring became unstable and dispersed into the ambient fluid. Thus, the experiments of Kojima *et al.* (1984) indicated that moving viscous drops are unstable when not protected by surface tension.

Kojima *et al.* (1984) undertook a theoretical investigation of the observed drop behaviour in the context of linear stability analysis and slender-body theory. They demonstrated that in the absence of surface tension, the spherical drop is indeed unstable to perturbations of small amplitude. Furthermore, they showed that the character of the evolution strongly depends on the type of initial perturbation. Unfortunately, these results were not able to explain all observed stages in the drop evolution, more specifically, the formation of drop rings from initially prolate drops. Even including weak inertial effects could not resolve all of the discrepancies between theory and experiment in a satisfactory manner. In a more recent study, Griffiths (1986) studied the evolution of thermals rising in quiescent fluid. He observed that the thermals became unstable, developing into axisymmetric drop rings, and noted that the effect of temperature-dependent viscosity plays a dominant role in the evolution. When repeating the experiments with isothermal drops, Griffiths obtained stable motion, in contrast to Kojima *et al.* (1984). The reason for this discrepancy is not known.

Overall, the experiments of Kojima *et al.* (1984) and Griffiths (1986) raised a number of fundamental questions regarding the precise mechanisms for drop evolution. In this paper we seek to obtain insight into these questions by studying the nonlinear instability of spherical drops. Our objectives are to probe the possible modes of deformation, to examine the significance of nonlinearities, and to assess the sensitivity of the evolution to the initial drop configuration, surface tension, and the ratio of the viscosity between the drop and the ambient fluid.

Our analysis relies on numerical solutions of the Stokes equation based on two different variations of the boundary-integral method for Stokes flow. The first variation, developed by Rallison & Acrivos (1978), uses the boundary-integral equation on either side of a fluid interface to represent the flow in terms of a combined distribution of Stokeslets and derivative singularities. The second variation is based on the representation of the flow by means of a interfacial distribution of Stokeslets. Both of these methods lead to Fredholm integral equations of the second kind whose numerical solution requires comparable computational effort. The second method, however, has the additional advantage that it is capable of producing the whole velocity field directly and solely from the computed Stokeslet distribution.

To solve the Fredholm integral equations resulting from the boundary-integral formulations, we develop an iterative numerical procedure. The main advantage of this procedure is that it requires $O(N^2 \times M)$ numerical operations, compared with $O(N^3)$ operations required by methods that are based on matrix inversions. Here N is the number of surface elements, and M is the number of necessary iterations, which in most cases is considerably less than N. Other advantages include ease of implementation and straightforward high-order discretization. The success of the

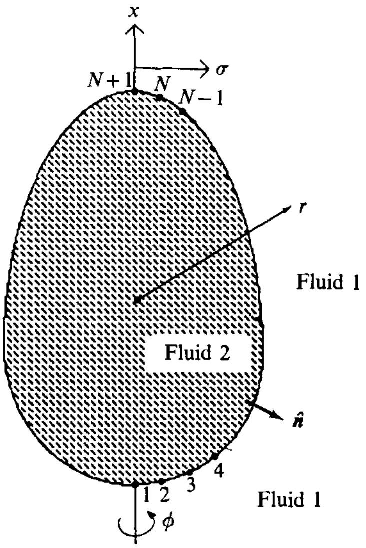

FIGURE 1. Defining sketch for an axisymmetric drop moving in an infinite ambient fluid.

proposed iterative method is due to the fact that the derived integral equations have convergent Neumann series, a property which is theoretically proven in Appendix A.

While this paper was under review, the author received a note by C. J. Koh & L. G. Leal, entitled 'The stability of drop shapes for translations at zero Reynolds number through a quiescent fluid'. The subject of this note is identical to that of the present study. The formulation of the problem is based on the method of Rallison & Acrivos, while the procedure of solution is based on matrix inversion (see also Stone & Leal 1989). The results of C. J. Koh & L. G. Leal are in excellent agreement with those presented in this paper.

The rest of our paper is structured as follows. In §2 we describe the basic flow configuration for the spherical drop, summarize the main conclusions of linear stability theory, formulate the complete nonlinear problem as an integral equation, and develop a numerical method of solution. In §3 we present and discuss our calculations. Section 4 contains concluding remarks.

2. Analysis

2.1. *The spherical drop*

Our basic flow configuration consists of a spherical drop moving under the influence of gravity in an ambient fluid of infinite extent. At the outset, we reduce all variables using as lengthscale the drop radius a, and as timescale $\mu_1/ag\Delta\rho$, where $\Delta\rho$ is the density difference $\rho_2-\rho_1$. A subscript 1 or 2 denotes the ambient or drop fluid, as indicated in figure 1. The speed of the drop is

$$U=-\frac{2}{3}\frac{1+\lambda}{1+3\lambda}, \tag{2.1}$$

where λ is the viscosity ratio μ_2/μ_1. The acceleration of gravity is in the direction of the negative x-axis. In the cylinder polar coordinates (x, σ, ϕ) of figure 1, and in a frame of reference moving with the drop, the axial and radial components of the velocity in the interior of the drop are

$$u_x = -\frac{1}{3}\frac{1}{2+3\lambda}(1-x^2-2\sigma^2), \quad u_\sigma -\frac{1}{3}\frac{1}{2+3\lambda}x\sigma. \tag{2.2a, b}$$

The azimuthal component of the vorticity is

$$\omega_\phi = -\frac{5}{3}\frac{1}{2+3\lambda}\sigma. \tag{2.2c}$$

Note that the velocity field inside the drop is identical to that inside Hill's spherical vortex, and thus it satisfies the complete Navier–Stokes equations. In spherical polar coordinates with origin at the centre of the drop, the velocity field outside the drop is given by

$$u_r = \frac{2}{3}\frac{x}{r}\left(\frac{1+\lambda}{2+3\lambda} - \frac{1}{2}\frac{1}{r} + \frac{\lambda}{2(2+3\lambda)}\frac{1}{r^3}\right), \tag{2.3a}$$

$$u_\theta = -\frac{1}{3}\frac{\sigma}{r}\left(2\frac{1+\lambda}{2+3\lambda} - \frac{1}{2}\frac{1}{r} - \frac{\lambda}{2(2+3\lambda)}\frac{1}{r^3}\right). \tag{2.3b}$$

One may recognize the far-field component, along with a *Stokeslet* with r^{-1}decay, and a *potential dipole* with r^{-3} decay, both oriented along the x-axis. The azimuthal component of the vorticity is exclusively due to the Stokeslet, and is given by

$$\omega_\phi = -\frac{1}{3}\frac{\sigma}{r^3}. \tag{2.3c}$$

It is well known that above flow field satisfies continuity of velocity and stress across the drop surface, independently of the magnitude of surface tension (Batchelor 1967, p. 235).

2.2. *Small deformation theory*

Kojima *et al.* (1984) analysed the evolution of small axisymmetric perturbations on the spherical drop at low Reynolds numbers. They studied the motion as a function of the form of the initial perturbation, viscosity ratio λ, and surface tension γ, the latter expressed by the inverse capillary number $N = \gamma/U\mu_1$. Specifically, they expanded the drop contour in a series of Legendre polynomials and, after linearizing the equations of motion and boundary conditions, they derived an infinite system of ordinary differential equations for the evolution of the coefficients in this series. Their analysis revealed that, in the absence of surface tension, the drop is unstable to infinitesimal perturbations. Prolate or oblate disturbances lead to formation of growing protrusions or intrusions at the rear stagnation point of the drop. The front of the drop always regains its unperturbed spherical shape. The timescale of the deformation is approximately proportional to $1+\lambda$. A small amount of surface tension is capable of suppressing the growth of small perturbations whose amplitude is commensurate with $1/N$. The viscosity ratio has little effect on the gross features of drop deformation. Furthermore, Kojima *et al.* showed that including weak inertial effects introduces a slight bias toward oblate-type evolutions, in the sense that slightly prolate perturbations amplify through the development of intrusions rather than protrusions at the rear of the drop.

2.3. *Formulation as an integral equation*

The theory of Kojima *et al.* (1984) is valid in the initial stages of the instability, as long as the drop maintains a slightly deformed shape. To describe the well-advanced stages of the evolution, and to examine the motion subject to perturbations of finite amplitude, we pursue an alternative formulation, one that is based on integral representations for Stokes flow. Below, we summarize the method of Rallison & Acrivos (1978), and then we present a new formulation.

In a study of drop deformation in uniaxial extensional flow, Rallison & Acrivos (1978) derived an integral equation for the evolution of the interface between two viscous fluids. Briefly, they applied the boundary-integral equation

$$(-1)^{\alpha+1}u_j(\boldsymbol{x}_0) = -\frac{1}{8\pi\mu_\alpha}\int_S f_i^{(\alpha)}(\boldsymbol{x})\,S_{ij}(\boldsymbol{x},\boldsymbol{x}_0)\,\mathrm{d}S(\boldsymbol{x}) + \frac{1}{8\pi}\int_S u_i(\boldsymbol{x})\,T_{ijk}(\boldsymbol{x},\boldsymbol{x}_0)\,\hat{n}_k(\boldsymbol{x})\,\mathrm{d}S(\boldsymbol{x}) \quad (2.4)$$

on either side of the interface, $\alpha = 1, 2$ (figure 1), and requiring continuity of velocity across the interface, they derived the following equation for the interfacial velocity:

$$u_j(\boldsymbol{x}_0) = -\frac{1}{4\pi\mu_1}\frac{1}{1+\lambda}\int_S \Delta f_i(\boldsymbol{x})\,S_{ij}(\boldsymbol{x},\boldsymbol{x}_0)\,\mathrm{d}S(\boldsymbol{x}) + \frac{\beta}{4\pi}\int_S^{I_{\mathrm{PV}}} u_i(\boldsymbol{x})\,T_{ijk}(\boldsymbol{x},\boldsymbol{x}_0)\,\hat{n}_k(\boldsymbol{x})\,\mathrm{d}S(\boldsymbol{x}). \quad (2.5)$$

In the above equations, $\hat{\boldsymbol{n}}$ is the unit vector normal to the interface pointing into fluid 1, I_{PV} indicates the principal-value Integral, β is a dimensionless parameter defined as $\beta = (1-\lambda)/(1+\lambda)$, and $\Delta \boldsymbol{f}$ is the difference in surface stress across the fluid interface. This is equal to $\Delta\boldsymbol{f} = (\boldsymbol{\sigma}_1 - \boldsymbol{\sigma}_2)\cdot\hat{\boldsymbol{n}}$ where $\boldsymbol{\sigma}$ is the modified stress tensor defined with respect to the modified pressure $P' = P - \rho_i \boldsymbol{g}\cdot\boldsymbol{x}$ (Batchelor 1967, p. 237). The tensors $\boldsymbol{S}$ and $\boldsymbol{T}$ are the Green's functions for the velocity and the stress respectively. Thus, $u_i = S_{ij}\alpha_j$, and $\sigma_{ik} = \mu T_{ijk}\alpha_j$ express the velocity and stress field produced by a point force of strength $8\pi\alpha_j$, located at the point $\boldsymbol{x}_0$. For unbounded three-dimensional flow, these tensors have the explicit forms

$$S_{ij}(\hat{\boldsymbol{x}}) = \frac{1}{|\hat{\boldsymbol{x}}|} + \frac{\hat{x}_i\hat{x}_j}{|\hat{\boldsymbol{x}}|^3}, \quad T_{ijk}(\hat{\boldsymbol{x}}) = -6\frac{\hat{x}_i\hat{x}_j\hat{x}_k}{|\hat{\boldsymbol{x}}|^5}, \quad (2.6a, b)$$

where $\hat{\boldsymbol{x}} = \boldsymbol{x} - \boldsymbol{x}_0$.

Specifying Δf, reduces (2.5) into a Fredholm integral equation of the second kind for the interfacial velocity. In the special case where the viscosities of the two fluids are equal ($\lambda = 1$ or $\beta = 0$), the second term on the right-hand side of this equation vanishes, and the velocity is simply expressed as an integral over the fluid interface. Once the interfacial velocity has been computed, by solving (2.5), the whole velocity field may be constructed by reverting to (2.4). To compute the first integral on the right-hand side of this equation, however one must know the surface stress $\boldsymbol{f}$ on either side of the fluid interface. This may be computed by applying (2.4) on one side of the interface, and then, by solving the resulting Fredholm integral equation of the first kind for $\boldsymbol{f}$. The surface stress on the other side of the interface is then immediately found from the known discontinuity in the interfacial surface stress $\Delta \boldsymbol{f}$. Thus, it appears that a complete computation of the flow field requires the solution of two integral equations, one of the second for the interfacial velocity, and the other of the first kind for the interfacial stress.

Solving the above integral equation for the boundary surface stress, however, is not necessary for the computation of the flow field. Indeed, the reciprocal theorem states that for a point $\boldsymbol{x}_0$ located in the interior of fluid 1, the following identity is true:

$$\int_S f_i^{(2)}(\boldsymbol{x})\, S_{ij}(\boldsymbol{x},\boldsymbol{x}_0)\,\mathrm{d}S(\boldsymbol{x}) - \mu_2 \int_S u_i(\boldsymbol{x})\, T_{ijk}(\boldsymbol{x},\boldsymbol{x}_0)\,\hat{n}_k(\boldsymbol{x})\,\mathrm{d}S(\boldsymbol{x}) = 0. \tag{2.7}$$

Applying (2.4) for $\alpha = 1$, and combining with (2.7) gives

$$u_j(\boldsymbol{x}_0) = -\frac{1}{8\pi\mu_1}\int_S \Delta f_i(\boldsymbol{x})\, S_{ij}(\boldsymbol{x},\boldsymbol{x}_0)\,\mathrm{d}S(\boldsymbol{x}) + \frac{1-\lambda}{8\pi}\int_S u_i(\boldsymbol{x})\, T_{ijk}(\boldsymbol{x},\boldsymbol{x}_0)\,\hat{n}_k(\boldsymbol{x})\,\mathrm{d}S(\boldsymbol{x}). \tag{2.8}$$

Effectively, the exterior flow is represented as a combined single-layer and double-layer potential with known density distribution functions. For a point $\boldsymbol{x}_0$ located in the interior of fluid 2, we write the identity

$$\int_S f_i^{(1)}(\boldsymbol{x})\, S_{ij}(\boldsymbol{x},\boldsymbol{x}_0)\,\mathrm{d}S(\boldsymbol{x}) - \mu_1 \int_S u_i(\boldsymbol{x})\, T_{ijk}(\boldsymbol{x},\boldsymbol{x}_0)\,\hat{n}_k(\boldsymbol{x})\,\mathrm{d}S(\boldsymbol{x}) = 0. \tag{2.9}$$

Applying (2.4) for $\alpha = 2$, and combining with (2.9) we obtain

$$u_j(\boldsymbol{x}_0) = -\frac{1}{8\pi\mu_1\lambda}\int_S \Delta f_i(\boldsymbol{x})\, S_{ij}(\boldsymbol{x},\boldsymbol{x}_0)\,\mathrm{d}S(\boldsymbol{x}) + \frac{1}{8\pi}\frac{1-\lambda}{\lambda}\int_S u_i(\boldsymbol{x})\, T_{ijk}(\boldsymbol{x},\boldsymbol{x}_0)\,\hat{n}_k(\boldsymbol{x})\,\mathrm{d}S(\boldsymbol{x}). \tag{2.10}$$

Thus, the interior flow is also represented as a combined single-layer and double-layer potential with known density distribution functions. As the point $\boldsymbol{x}_0$ approaches the interface S, the double layers in (2.8) and (2.10) may be written in terms of their corresponding principal values, and both (2.8) and (2.10) reduce to the Rallison & Acrivos equation (2.5).

In an alternative formulation, we represent the velocity in terms of a single-layer distribution of Stokeslets over the fluid interface

$$u_i(\boldsymbol{x}_0) = \int_S S_{ij}(\boldsymbol{x}_0,\boldsymbol{x})\, q_j(\boldsymbol{x})\,\mathrm{d}S(\boldsymbol{x}), \tag{2.11}$$

where $\boldsymbol{q}$ is the density of the distribution. The associated stress field is given by

$$\sigma_{ik}(\boldsymbol{x}_0) = \mu_\alpha \int_S T_{ijk}(\boldsymbol{x}_0,\boldsymbol{x})\, q_j(\boldsymbol{x})\,\mathrm{d}S(\boldsymbol{x}). \tag{2.12}$$

The surface stress on either side of the interface is equal to

$$(f_i)_\alpha(\boldsymbol{x}_0) = \sigma_{ik}(\boldsymbol{x}_0)\,\hat{n}_k(\boldsymbol{x}_0) = \mu_\alpha\,\hat{n}_k(\boldsymbol{x}_0)\int_S T_{ijk}(\boldsymbol{x}_0,\boldsymbol{x})\, q_j(\boldsymbol{x})\,\mathrm{d}S(\boldsymbol{x}), \tag{2.13}$$

where $\alpha = 1, 2$. As the interface is crossed, the integral on the right-hand side suffers a discontinuity equal to $-8\pi\boldsymbol{q}$. Introducing the principal-value integral, equal to the mean value of the integral on either side of the interface, we rewrite the two limiting values of the surface stress as

$$(f_i)^1(\boldsymbol{x}_0) = -4\pi\mu_1\, q_i(\boldsymbol{x}_0) + \mu_1\,\hat{n}_k(\boldsymbol{x}_0)\int_S^{\mathcal{P}\mathrm{V}} T_{ijk}(\boldsymbol{x}_0,\boldsymbol{x})\, q_j(\boldsymbol{x})\,\mathrm{d}S(\boldsymbol{x}), \tag{2.14a}$$

$$(f_i)^2(\boldsymbol{x}_0) = 4\pi\mu_2\, q_i(\boldsymbol{x}_0) + \mu_2\,\hat{n}_k(\boldsymbol{x}_0)\int_S^{\mathcal{P}\mathrm{V}} T_{ijk}(\boldsymbol{x}_0,\boldsymbol{x})\, q_j(\boldsymbol{x})\,\mathrm{d}S(\boldsymbol{x}). \tag{2.14b}$$

Subtracting these equations, we find

$$q_i(\boldsymbol{x}_0) = -\frac{1}{4\pi\mu_1(1+\lambda)}\Delta f_i(\boldsymbol{x}_0) + \frac{\beta}{4\pi}\hat{n}_k(\boldsymbol{x}_0)\int_S^{I_{\mathrm{PV}}} T_{ijk}(\boldsymbol{x}_0, \boldsymbol{x})\, q_j(\boldsymbol{x})\,\mathrm{d}S(\boldsymbol{x}). \tag{2.15}$$

When the viscosities of the two fluids are equal ($\lambda = 1$ or $\beta = 0$), we obtain

$$q_i = -\frac{1}{8\pi\mu}\Delta f_i.$$

This renders (2.11) equivalent to (2.5). In the general case of unequal viscosities, (2.15) constitutes a Fredholm integral equation of the second kind for $\boldsymbol{q}$. Solving for $\boldsymbol{q}$ allows the direct computation of the velocity field within either fluid, using the defining expression (2.11).

Comparing the above two formulations, we find that the second one offers two significant advantages. First, it produces the velocity field solely from a single-layer Stokeslet distribution. Second, this formulation is based on the integral representation (2.11) which is valid both inside and outside the drop. Thus, it allows the computations of the velocity at a point, without requiring information on whether this point is located inside or outside the drop.

Before proceeding further with the integral equations (2.5) and (2.15), it is imperative to examine the uniqueness of their solution. For this purpose, we consider the corresponding homogeneous equations,

$$u_i(\boldsymbol{x}_0) = \frac{\beta}{4\pi}\int_S^{I_{\mathrm{PV}}} u_j(\boldsymbol{x})\, T_{jik}(\boldsymbol{x}, \boldsymbol{x}_0)\,\hat{n}_k(\boldsymbol{x})\,\mathrm{d}S(\boldsymbol{x}), \tag{2.16a}$$

$$q_i(\boldsymbol{x}_0) = \frac{\beta}{4\pi}\hat{n}_k(\boldsymbol{x}_0)\int_S^{I_{\mathrm{PV}}} T_{ijk}(\boldsymbol{x}_0, \boldsymbol{x})\, q_j(\boldsymbol{x})\,\mathrm{d}S(\boldsymbol{x}) \tag{2.16b}$$

and inquire whether they have non-trivial characteristic solutions. Note that (2.16*a*) and (2.16*b*) are adjoint to each other, and thus they have conjugate eigenvalues and the same number of eigensolutions. Now, it is well known that when the drop becomes a frictionless bubble, $\lambda = 0$ or $\beta = 1$, these equations have a single eigensolution, and when the drop becomes a solid particle, $\lambda = \infty$ or $\beta = -1$, they have six independent eigensolutions (Ladyzhensakya 1969, p. 60). Power (1987) showed that in the intervening region $0 < \lambda < \infty$ or $-1 < \beta < 1$, (2.16*a*) and (2.16*b*) have no eigensolutions (see also Appendix A). This ensures that both (2.5) and (2.15) have unique solutions.

To complete our formulation we must define a constitutive equation for the discontinuity of the surface stress $\Delta\boldsymbol{f}$. Assuming that the surface tension is constant along the fluid interface, we write

$$\Delta\boldsymbol{f} = (\Delta\rho g x + \gamma\boldsymbol{\nabla}\cdot\hat{\boldsymbol{n}})\,\hat{\boldsymbol{n}}. \tag{2.17}$$

Substituting into (2.5), and reducing lengths by the equivalent drop radius a, velocities by $g\Delta\rho a^2/\mu_1$, and stresses by $g\Delta\rho$, we obtain

$$u_j(\boldsymbol{x}_0) = -\frac{1}{4\pi(1+\lambda)}\int_S (x + \Gamma\boldsymbol{\nabla}\cdot\hat{\boldsymbol{n}})\,\hat{n}_i(\boldsymbol{x})\,S_{ij}(\hat{\boldsymbol{x}})\,\mathrm{d}S(\boldsymbol{x}) + \frac{\beta}{4\pi}\int_S^{I_{\mathrm{PV}}} u_i(\boldsymbol{x})\,T_{ijk}(\hat{\boldsymbol{x}})\,\hat{n}_k(\boldsymbol{x})\,\mathrm{d}S(\boldsymbol{x}). \tag{2.18}$$

Γ is the inverse Bond number, $\Gamma = \gamma/a^2\Delta\rho g$, related to the inverse capillary number $N = \gamma/\mu U$ by $\Gamma = 2N(1+\lambda)/(6+9\lambda)$. Furthermore, substituting (2.17) into (2.15), we find

$$q_i(\boldsymbol{x}_0) = -\frac{1}{4\pi(1+\lambda)}[x_0+\Gamma\boldsymbol{\nabla}_0\cdot\hat{\boldsymbol{n}}]\,\hat{n}_i(\boldsymbol{x}_0)-\frac{\beta}{4\pi}\hat{n}_k(\boldsymbol{x}_0)\int_S^{I_{\mathrm{PV}}} T_{ijk}(\hat{\boldsymbol{x}})\,q_j(\boldsymbol{x})\,\mathrm{d}S(\boldsymbol{x}). \quad (2.19)$$

The problem is reduced to solving (2.18) or (2.19) for the interfacial velocity or for the density of the distribution density $\boldsymbol{q}$.

2.4. *Numerical solution of the integral equations*

In this section we develop a numerical procedure for solving the integral equations (2.18) or (2.19) for the case of axisymmetric motion. To facilitate our discussion, we rewrite (2.18) in the equivalent form

$$u_j(\boldsymbol{x}_0) = -\frac{1}{4\pi(1+\lambda)}A_j(\boldsymbol{x}_0)+\frac{\beta}{4\pi}B_j(\boldsymbol{x}_0), \quad (2.20)$$

where the integrals $\boldsymbol{A}$ and $\boldsymbol{B}$ represent single-layer and double-layer potentials. The standard procedure for solving this equations, employed by all previous investigators, is by means of boundary discretization, followed by collocation and matrix inversion (Delves & Mohamed 1985). Briefly, this entails (i) discretization of the drop surface into a set of N boundary elements, (ii) approximation of the velocity distribution over each element with a polynomial function, and (iii) computation of the polynomial coefficients. This last step is effected by applying the equation at selected collocation points on the drop surface. In this manner, the problem is reduced to solving a dense system of linear equations of $O(N^2)$, requiring $O(N^3)$ arithmetic operations, and $O(N^2)$ computer storage.

Motivated by the success of iterative methods for solving Fredholm integral equations of the second kind for problems of potential flow (Baker, Meiron & Orszag 1982), we develop an alternative method of solution, one that is based on successive iterations. Our strategy is to assume an arbitrary interfacial velocity distribution, to compute the right-hand side of (2.20), and then to replace that originally assumed with the newly computed velocity distribution. The basic advantage of this method is that it requires $O(N^2\times M)$ arithmetic operations, where M is the number of iterations. When M is less than N, this results in significant savings in the cost of the computations. Other important advantages include ease of implementation, and efficiency in handling the singular integrals $\boldsymbol{A}$ and $\boldsymbol{B}$. To ensure the success of our iterative method of solution, in Appendix A we show that the Neumann series of the integral equations (2.18) and (2.20) are convergent by proving that the corresponding homogeneous equations (2.16*a*, *b*) do not have any real or complex eigenvalues with magnitude less than one (Korn & Korn 1968, p. 497).

Proceeding with the numerical implementation, we note that both of the integrals in (2.20) are singular, their integrands exhibiting a logarithmic and a polar singularity as $\boldsymbol{x}\rightarrow\boldsymbol{x}_0$. The former must be treated numerically, but the latter may be removed by using the identity

$$\int_S^{I_{\mathrm{PV}}} T_{ijk}(\boldsymbol{x},\boldsymbol{x}_0)\,\hat{n}_k(\boldsymbol{x})\,\mathrm{d}S(\boldsymbol{x}) = -4\pi\delta_{ij} \quad (2.21)$$

(this may be derived by applying the boundary-integral equation (2.4) for a uniform flow in the interior of S, that is, with $\boldsymbol{u}$ equal to a constant and $\boldsymbol{f}$ proportional to the normal vector). We thus write

$$B_j(\boldsymbol{x}_0) \equiv \int_S^{I_{\mathrm{PV}}} u_i(\boldsymbol{x})\, T_{ijk}(\hat{\boldsymbol{x}})\, \hat{n}_k(\boldsymbol{x})\, \mathrm{d}S(\boldsymbol{x}) \equiv C_j(\boldsymbol{x}_0) - 4\pi u_j(\boldsymbol{x}_0), \tag{2.22}$$

where

$$C_j(\boldsymbol{x}_0) = \int_S [u_i(\boldsymbol{x}) - u_i(\boldsymbol{x}_0)]\, T_{ijk}(\hat{\boldsymbol{x}})\, \hat{n}_k(\boldsymbol{x})\, \mathrm{d}S(\boldsymbol{x}). \tag{2.23}$$

The integral on the right-hand side of (2.23) is computed using the six-point Gauss–Legendre quadrature.

For axisymmetric flow, we perform the integration in the azimuthal direction to express the above integrals in terms of complete elliptic integrals of the first and second kind. Referring to cylindrical polar coordinates we write

$$A_\alpha(\boldsymbol{x}_0) = -\int_C (x + \Gamma \boldsymbol{\nabla} \cdot \hat{\boldsymbol{n}}) M_{\alpha\beta}(\boldsymbol{x}, \boldsymbol{x}_0)\, \hat{n}_\beta(\boldsymbol{x})\, \mathrm{d}l(\boldsymbol{x}), \tag{2.24a}$$

$$C_\alpha(\boldsymbol{x}_0) = \int_S \{q_{\alpha 1\beta}(\boldsymbol{x}, \boldsymbol{x}_0)\, [u_1(\boldsymbol{x}) - u_1(\boldsymbol{x}_0)] + q_{\alpha 2\beta}(\boldsymbol{x}, \boldsymbol{x}_0)\, u_2(\boldsymbol{x}) \\ - p_{\alpha\beta}(\boldsymbol{x}, \boldsymbol{x}_0)\, u_2(\boldsymbol{x}_0)\}\, \hat{n}_\beta(\boldsymbol{x})\, \mathrm{d}l(\boldsymbol{x}), \tag{2.24b}$$

where the integration is along the contour of the drop in a meridional plane. Greek subscripts take the values (1, 2) for the (x, σ) directions respectively. It was necessary to introduce three new matrices $\boldsymbol{M}$, $\boldsymbol{q}$, and $\boldsymbol{p}$, whose elements are given in appendix B, in a form suitable for computer implementation.

In our numerical procedure, we trace the contour of the drop with a set of $N+1$ marker points, and approximate the shape of the drop with a set of circular arcs passing through successive trios of marker points (figure 1). The curvature of the drop over an arc is computed by

$$\boldsymbol{\nabla} \cdot \hat{\boldsymbol{n}} = \frac{\pm 1}{R} + \frac{\hat{\boldsymbol{n}} \cdot \boldsymbol{j}}{\sigma}, \tag{2.25}$$

where $\boldsymbol{j}$ is the unit vector in the σ-direction, and the plus or minus sign reflects the counterclockwise or clockwise arc orientation. To compute $\boldsymbol{A}$, we subtract off, and integrate analytically the logarithmic singularity over the arc hosting a marker point. To compute $\boldsymbol{C}$, we evaluate $\boldsymbol{M} \cdot \boldsymbol{n}$, $\boldsymbol{q} \cdot \boldsymbol{n}$, and $\boldsymbol{p} \cdot \boldsymbol{n}$ at the Gaussian points over each arc, multiply them by the corresponding Gauss–Legendre weights, and save them in a $N \times N \times m$ matrix (m is the number of the quadrature points). We then assume a trial velocity at the marker points, approximate the velocity distribution over each are with a parabolic function with respect to arc length, and compute the velocity at the quadrature points. Finally, we compute $\boldsymbol{C}$ simply by multiplying its kernel with the velocity at the quadrature points and summing. Having computed $\boldsymbol{A}$ and $\boldsymbol{C}$, we calculate the new values of the velocity at the marker points, and repeat the procedure until the difference in the velocity between the two successive iterates at all points differs only by a predetermined small number. The above strategy allows the evaluation of the integral $\boldsymbol{C}$ for different velocity distributions, without requiring the costly computation of the kernel each time. Once the interfacial velocity is obtained, the position of the marker points is advanced using the modified Euler's method.

To accelerate the convergence of the iterations, we set the initial guess for the velocity equal to the converged velocity at the previous time step. In our computations, we found that the required number of iterations is strongly dependent on the viscosity ratio and the specified accuracy, while it is quite insensitive to the number of boundary elements N. For instance, for absolute accuracy of 10^{-8}, the number of necessary iterations varied from eight for $\lambda = 0.50$, to forty for $\lambda = 0.10$ and 10.

To solve (2.19), we devise a procedure similar to that described above. Specifically, to compute the singular integral on the right-hand side of (2.19), we rewrite it in the form

$$\int_S h_{jik}(\boldsymbol{x}_0, \boldsymbol{x})\,[q_i(\boldsymbol{x})\,\hat{n}_k(\boldsymbol{x}_0) - q_k(\boldsymbol{x}_0)\,\hat{n}_i(\boldsymbol{x})]\,\mathrm{d}l(\boldsymbol{x}) - 4\pi q_j(\boldsymbol{x}_0) \tag{2.26}$$

where the integration is over the drop contour in a meridional plane. The matrix $\boldsymbol{h}$ is given in Appendix B. The integral in (2.26) is regular, and is evaluated using the Gauss–Legendre quadrature.

The need for point redistribution arises when regions of high curvature develop, and when the marker points move far apart from each other or cluster at regions of low curvature. To maintain an acceptable point distribution which is capable of resolving the fine scales of the motion, but yet does not require an excessive number of points, we use an adaptive method of point redistribution based on three criteria. First, when the total angle subtended by an arc exceeds a specified maximum, we introduce two points evenly spaced along the arc, and remove the middle point. Second, when the separation between two points becomes excessively large, we introduce a point in the middle between these points. Third, when the separation between two points becomes smaller than a pre-established minimum, we eliminate these points, and introduce a new single new point located in the middle between the old points. This last operation is permissible only when the resulting point distribution does not violate the first two criteria. In all cases, the necessary interpolations are performed over the two arcs that are defined on either side of the segment connecting two adjacent points.

In the course of computations with zero surface tension, we observed the development of regions of high curvature, requiring a locally dense distribution of points. To maintain the number of points moderate, we allowed the formation of corners at these regions. Test calculations showed that this simplification did not have noticeable effect on the overall dynamics of the motion. The maximum number of points in our computations was 100 for fluids of equal viscosity, and 50 for fluids of different viscosity. When surface tension was equal to zero, the computations proceeded smoothly. When surface tension was finite, however, numerical instabilities arose, causing the interface to obtain a saw-tooth shape. These instabilities, similar in nature to those observed by other authors (Rallison 1984), were suppressed by decreasing the time step to a sufficiently low level.

To monitor the accuracy of the calculations, after each time step we computed the drop volume. The maximum change in this volume was less than 0.20% for $\lambda = 1$, and less than 1% for $\lambda \neq 1$. All of our computations were carried out using the formulation of Rallison & Acrivos. The instantaneous velocity field and streamline patterns were computed using the method of Stokeslet distribution. All computations were performed on the CRAY/XM-P computer of the San Diego Supercomputer Center. A complete run required approximately 30 min of CPU time.

3. Nonlinear drop evolution

In this section we study the nonlinear evolution of a perturbed spherical drop having an initial shape of a prolate or an oblate spheroid. The initial contour of the drop in a meridional plane is described by

$$r = \alpha[1+\epsilon P_2(\cos\theta)], \tag{3.1}$$

where P_2 is the second-degree Legendre polynomial, and α is a function of ϵ such that the drop volume is equal to $\frac{4}{3}\pi$. In this fashion, all lengths are reduced by the equivalent drop radius $a = (3V/4\pi)^{\frac{1}{3}}$. The evolution of the drop is a function of the perturbation amplitude ϵ, the inverse Bond number Γ, and the viscosity ratio λ. In our discussion, we pursue the motion in a frame of reference moving with the undisturbed drop velocity U (see §2.1). The unit of time is equal to $\mu_1/ag\Delta\rho$.

Figure 2(*a–i*) illustrates the evolution of a drop subjected to a prolate perturbation of amplitude $\epsilon = 0.200$. The viscosity ratio λ is equal to one, and the surface tension is equal to zero. The dotted contours in frames 2(*b–d*) represent predictions of linear theory. Overall, we discern three stages in the evolution. In the first stage, illustrated in frames 2(*a–c*), the front of the drop tends to recover its undisturbed spherical shape, whereas the rear of the drop is extended under the action of the local stagnation-point flow. During this stage, fluid from the front of the drop is convected towards the rear of the drop. Linear theory is remarkably accurate during this stage of deformation. In the second stage, illustrated in frames 2(*d–f*), fluid escapes from the main body of the drop into a developing tail. At the same time, ambient fluid is entrained into the drop near the base of the tail. Linear theory becomes increasingly less accurate during this stage of deformation. In the third stage, depicted in figure 2(*g–i*), the tail is stretched by the external flow, reducing into an elongated fluid thread. The ambient fluid that has been entrained into the drop is convected by the internal flow in a spiral pattern. The calculations strongly suggest that at large times, the drop reaches an asymptotic configuration. This is composed of an almost spherical body, a thin filament of ambient fluid that circulates inside the drop, and a tail that suffers continuous elongation. Inspection of frame 2(*i*) indicates the development of a spike at the rear of the drop, right above the base of the tail. In reality, this is a thin cylindrical filament of drop fluid which is passively convected by the external flow. It is worth noting that in the frame of reference of figure 2, the drop moves downward at a slow rate, implying that in a static frame of reference, the drop slightly decelerates during its evolution.

To illustrate the effect of viscosity ratio, in figure 3(*a*, *b*) we present two characteristic stages in the evolution of a drop with $\epsilon = 0.200$, $\lambda = 5$, and $\Gamma = 0$. These may be compared with the corresponding stages for $\lambda = 1$, shown in figures 2(*f*) and 2(*h*). We observe that increasing λ increases the size of the developing tail, and causes the entrained ambient fluid to penetrate the drop farther away from the axis of motion. Furthermore, increasing λ suppresses or delays drop filamentation. To further demonstrate the effect of the viscosity ratio, in figure 4 we present an advanced evolution stage for $\lambda = 0.10$, $\epsilon = 0.20$, and $\Gamma = 0$. We note that the size of the tail is significantly reduced with respect to that for $\lambda = 1$. Furthermore, we note the formation of a pronounced spike near the base of the tail, a precursor of drop filamentation.

Let us now examine the motion in a more quantitative fashion. For convenience, we characterize the drop deformation by a single variable d, equal to the size of the drop along the axis of motion. Linear theory predicts that d increases exponentially

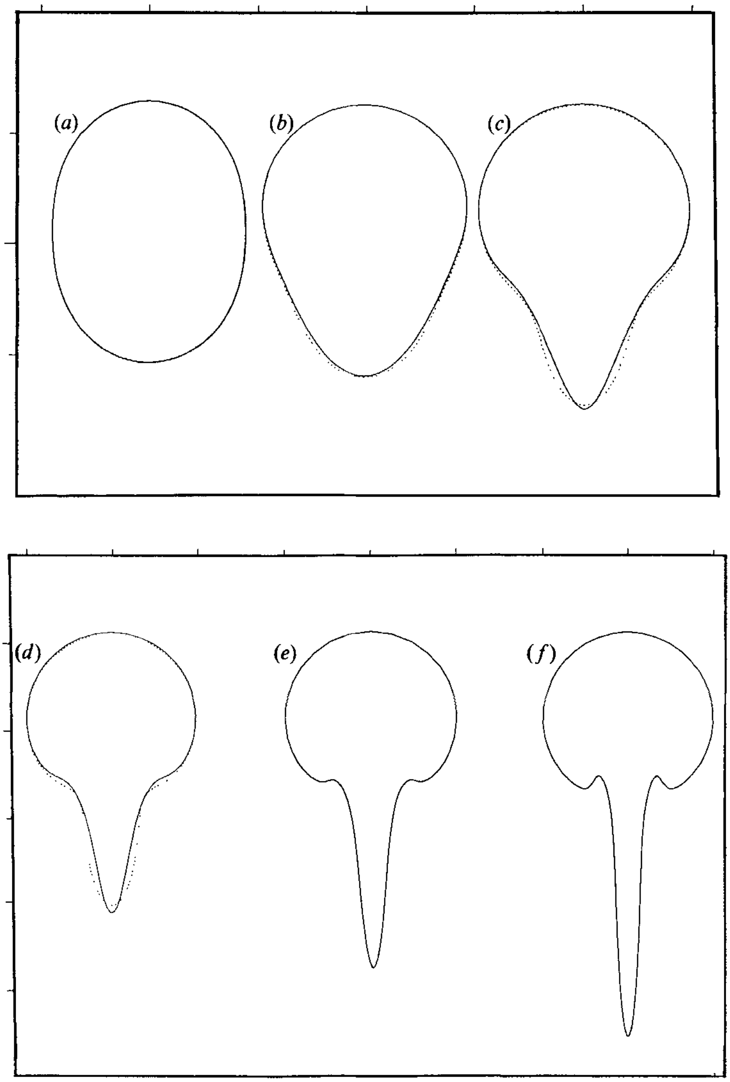

FIGURE 2(*a–f*). For caption see facing page.

in time, with a time constant proportional to $a(1+\lambda)/U$. Maintaining this scaling for lack of a better alternative, in figure 5 we plot d as a function of the non-dimensional time $t^* = tU/a(1+\lambda)$, for $\epsilon = 0.20$, $\Gamma = 0$, and three viscosity ratios $\lambda = 0.10$, 1.0, and 5.0 (solid lines). In all cases, we observe an initial exponential growth followed by a linear growth with slope very close to $\lambda + 1$. This reflects the fact that, at large times, the tail of the drop is convected by the external flow as a passive element. In figure 5, with dotted lines, we also show predictions of linear theory. This is accurate approximately up to $t^* = 2.0$, while the deformation of the drop is still moderate, but fails at later times.

Proceeding, we examine the effect of surface tension. In figure 6(*a–e*) we present characteristic stages in the evolution of an initially prolate drop with $\epsilon = 0.20$, for $\Gamma = 0.050$, and for fluids with equal viscosity $\lambda = 1$. The main features of the evolution are similar to those for zero surface tension presented in figure 2. It is clear,

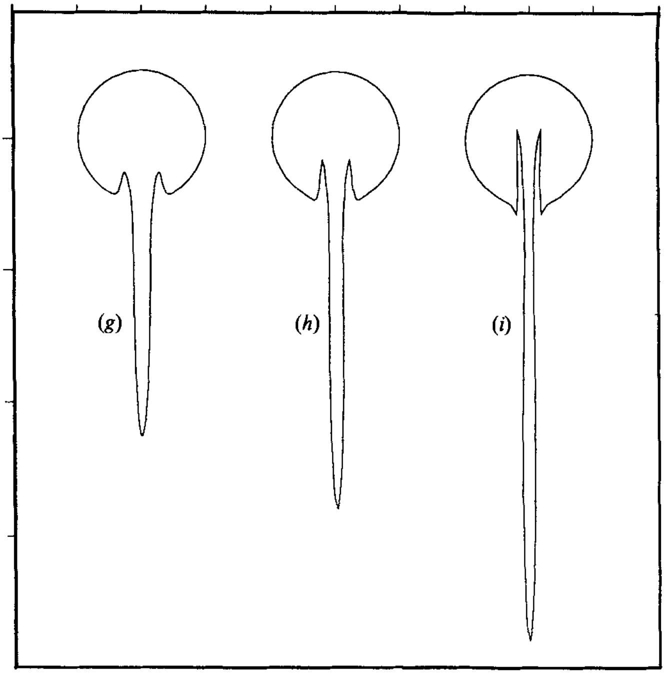

FIGURE 2. The evolution of an initially prolate drop with $\epsilon = 0.200$, for viscosity ratio $\lambda = \mu_2/\mu_1 = 1$, and surface tension $\Gamma = 0$: (*a*) $t = 0$, (*b*) 8.0, (*c*) 15.0, (*d*) 20, (*e*) 25.0, (*f*) 30.0, (*g*) 35.10, (*h*) 40.70, (*i*) 50.20. The dotted contours indicate predictions of linear theory with origin at the centre of mass of the drop.

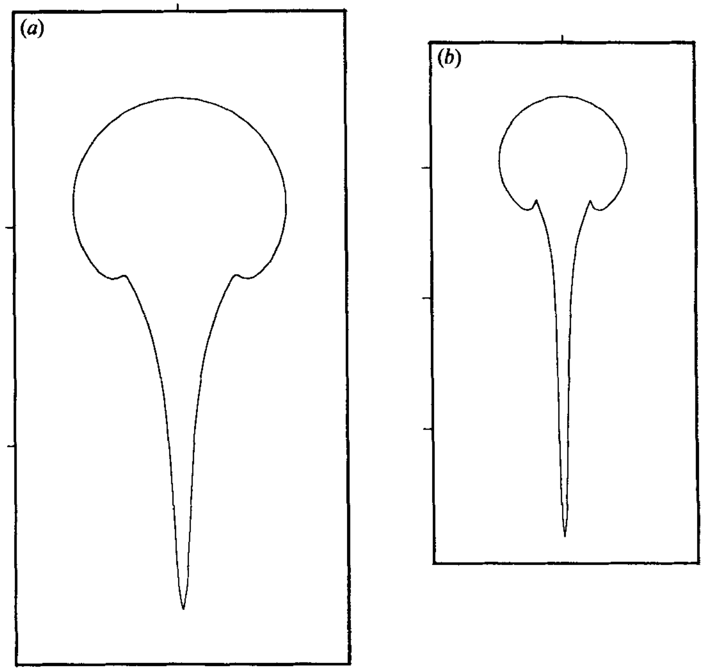

FIGURE 3. Two characteristic stages in the evolution of an initially prolate drop of amplitude $\epsilon = 0.20$, for viscosity ratio $\lambda = \mu_2/\mu_1 = 5.0$, and surface tension $\Gamma = 0$: (*a*) $t = 76.50$, (*b*) 90.50. To assess the effect of increasing the viscosity ratio, (*a*) should be compared with figure 2(*f*) and (*b*) with figure 2(*h*).

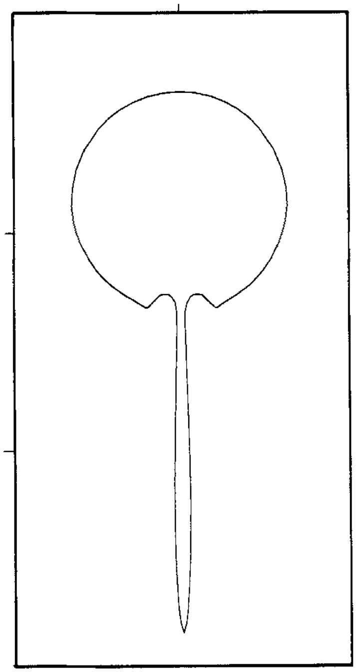

FIGURE 4. The drop shape at $t = 18.0$ for viscosity ratio $\lambda = 0.10$, surface tension $\Gamma = 0$, and for a perturbation of initial amplitude $\epsilon = 0.200$.

however, that surface tension prevents entrainment of ambient fluid and prohibits drop filamentation. Calculations beyond the time of figure 6 (*e*) indicated that the tail breaks up into a number of small drops. Whether this behaviour is a consequence of a numerical instability or a result of a real capillary instability however, could not be resolved with confidence. Comparing our numerical results with predictions of linear theory (illustrated with dotted lines in figure 6 (*b*, *c*), we see fair agreement at small times, but severe discrepancies at intermediate and large times. This is not surprising, for linear theory predicts that at large times the drop returns to its unperturbed spherical shape, whereas our nonlinear calculation show continuous deformation. To further investigate the effect of surface tension, we carried out computations with Γ equal to 0.100, 0.200, and $\epsilon = 0.200$. In the first case the perturbation grew as shown in figure 2, whereas in the second case, the perturbation decayed and the drop regained its unperturbed spherical shape.

We now turn our attention to oblate perturbations, concentrating on the case $\epsilon = -0.200$. In figure 7 (*a–f*) we summarize typical stages in the evolution of a drop for $\lambda = 1$ and $\Gamma = 0$. The dashed lines indicate predictions of linear theory. As in the case of prolate perturbations, the evolution of the drop proceeds in three distinct stages. During the first stage, shown in frames 7 (*a–c*), a dimple develops at the rear of the drop, while the front of the drop recovers its unperturbed spherical shape. Linear theory is accurate up to the time of figure 7 (*b*). In the second stage, shown in frames 7 (*d–f*), ambient fluid is entrained into the drop along the axis of the dimple. In this manner, the drop reduces into a ring. At the same time, a small filament of drop fluid develops right above the dimple. At large times, the drop reduces into a nearly symmetric steadily translating drop ring. In the frame of reference of figure 7, the

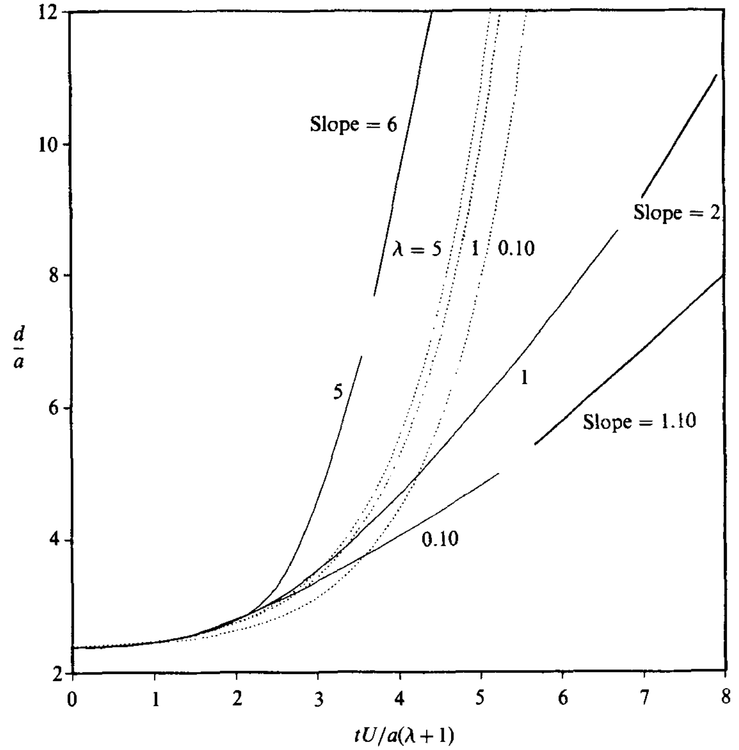

FIGURE 5. The size of the drop in the streamwise direction, d, as a function of the non-dimensional time $tU/a(\lambda+1)$, this scaling suggested by linear theory. The initial amplitude of the perturbation is $\epsilon = 0.200$, and the surface tension $\Gamma = 0$. The dotted lines indicate predictions of the linear theory of Kojima *et al.* (1984); the slopes of the straight lines are equal to $\lambda + 1$, corresponding to the tail being convected at the undisturbed drop speed U.

drop moves upward at a slow rate, implying that in a static frame of reference, the drop undergoes slight acceleration during its evolution.

To illustrate the effect of λ on the growth of oblate perturbations, in figure 8 we present a characteristic advanced stage in the evolution of a drop for $\epsilon = -0.200$, $\lambda = 5.0$, and $\Gamma = 0$. Superposed on the drop contour is the instantaneous streamline pattern. Comparing figure 8 to figure 7 shows that increasing λ prevents drop filamentation, and causes a reduction in the amount of entrained ambient fluid. At large times, the drop is expected to reduce into an almost-steady drop ring similar to that developed for $\lambda = 1$. Furthermore, in figure 9(*a*, *b*), we present two characteristic stages in the evolution of a drop for $\epsilon = -0.20$, $\lambda = 0.10$, and $\Gamma = 0$. A notable new feature is the spherical-cap shape of the dimple developing at the rear of the drop (figure 9(*a*)). The high-viscosity fluid residing within this dimple is subjected to a local extensional flow, and thus it undergoes slow deformation. The low-viscosity drop fluid above the dimple undergoes intense filamentation. The instantaneous streamline shown in figure 9(*a*) suggests that at large times, the drop reduces into a ring.

To illustrate the effect of surface tension for oblate perturbations, in figure 10(*a*–*f*) we present typical stages in the evolution of a drop for $\epsilon = -0.200$, $\lambda = 1$, and $\Gamma = 0.050$. The main features of the evolution are similar to those for $\Gamma = 0$, shown in

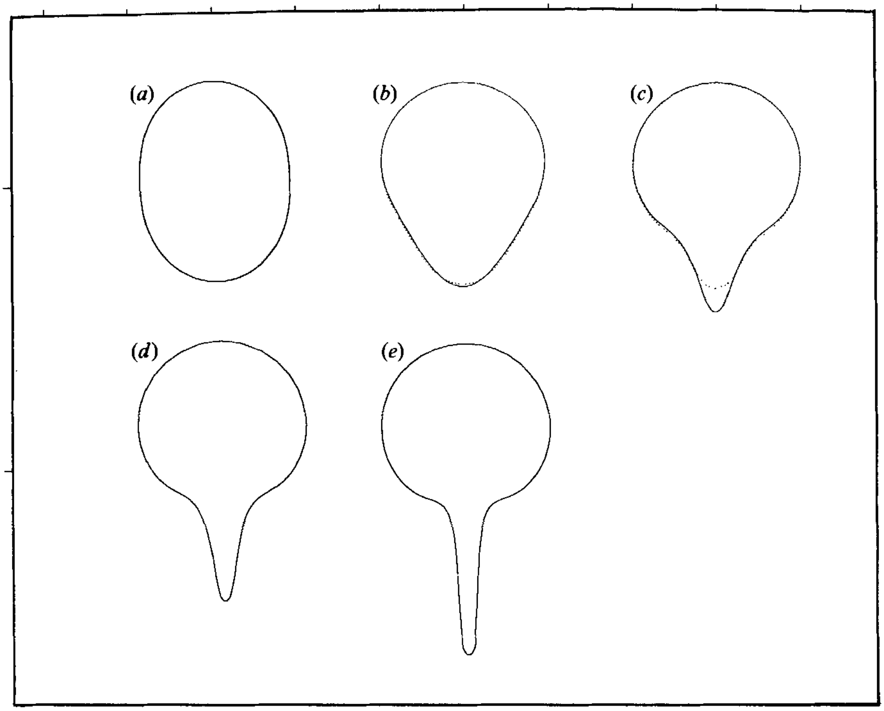

FIGURE 6. The effect of surface tension on the growth of prolate perturbations. The initial amplitude of the perturbation is $\epsilon = 0.200$, the viscosity ratio is $\lambda = \mu_2/\mu_1 = 1$, and the surface tension $\Gamma = 0.050$: (*a*) $t = 0$, (*b*) 10.0, (*c*) 20.0, (*d*) 25.0, (*e*) 30.70; this figure should be compared with figure 2. The dotted contours indicate predictions of linear theory with origin at the centre of mass of the drop.

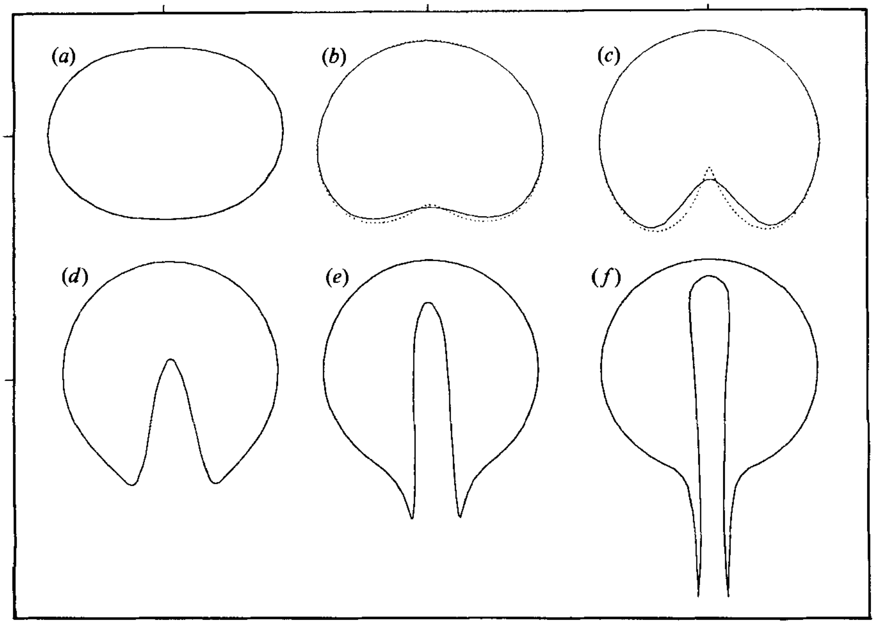

FIGURE 7. The evolution of an initially oblate drop, with perturbation amplitude $\epsilon = -0.20$, for viscosity ratio $\lambda = \mu_2/\mu_1 = 1$, and surface tension $\Gamma = 0$: (*a*) $t = 0$, (*b*) 8.0, (*c*) 15.0, (*d*) 25.0, (*e*) 35.0, (*f*) 45.0. The dotted contours indicate predictions of linear theory with origin at the centre of mass of the drop.

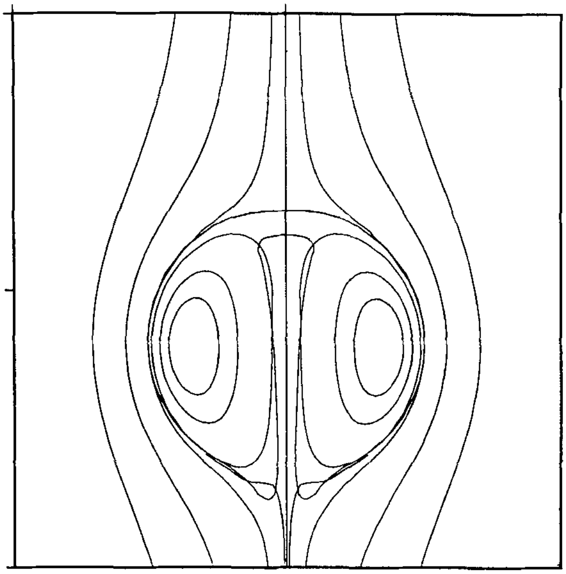

FIGURE 8. The shape of the drop and instantaneous streamline pattern at $t = 122.50$, for viscosity ratio $\lambda = 5.00$, surface tension $\Gamma = 0$. The initial amplitude of the perturbation is $\epsilon = -0.20$.

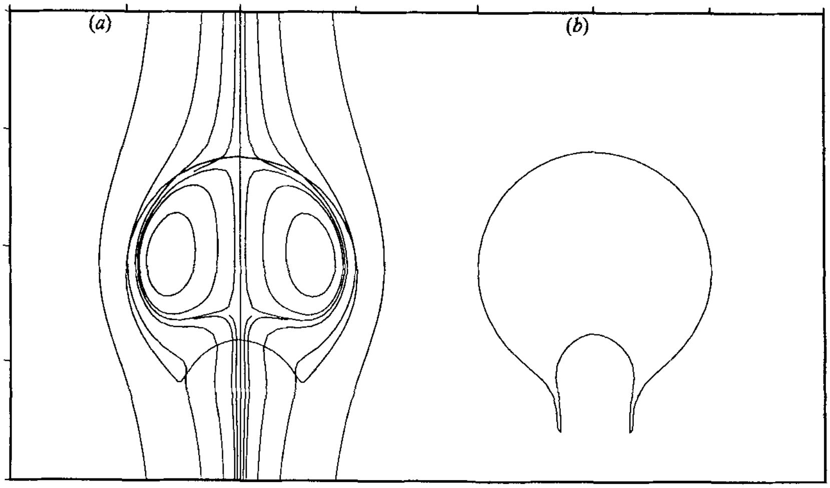

FIGURE 9. Two characteristic stages in the evolution of an initially oblate drop of amplitude $\epsilon = -0.200$, for viscosity ratio $\lambda = \mu_2/\mu_1 = 0.10$, and surface tension $\Gamma = 0$: (a) $t = 10.80$, (b) 17.00; superimposed in the drop contour in (a) is the instantaneous streamline pattern in a frame of reference moving with the undisturbed spherical drop speed U.

figure 6. Linear theory erroneously predicts that the drop gains its spherical shape at large times. Our computations show that the asymptotic drop shape consists of a compact, nearly spherical drop that encloses a spike of entrained ambient fluid. As in the case of prolate perturbations, drop filamentation is prevented by the presence of surface tension. Further calculations showed that increasing Γ to 0.100, while maintaining $\epsilon = -0.200$, stabilizes the drop, causing it to revert to its undisturbed spherical configuration.

In the above discussion we presented results for two specific perturbation

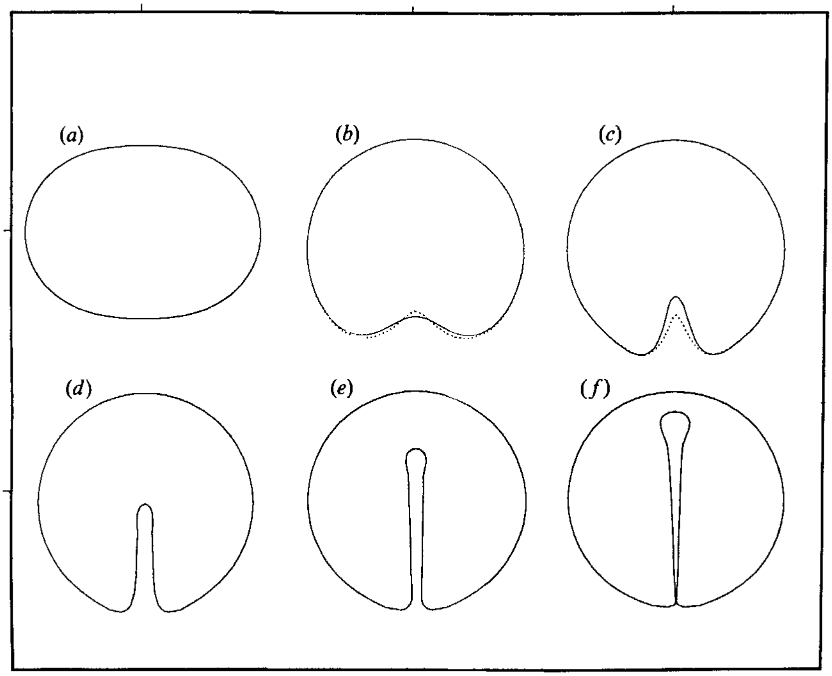

FIGURE 10. The effect of surface tension: evolution of an initially oblate drop of amplitude $\epsilon = -0.200$, for viscosity ratio $\lambda = \mu_2/\mu_1 = 1$, and $\Gamma = 0.050$: (*a*) $t = 0$, (*b*) 15.0, (*c*) 30.0, (*d*) 40.0, (*e*) 50.0 (*f*) 61.50. This figure should be compared with figure 6. The dotted contours indicate predictions of linear theory with origin at the drop centre of mass.

amplitudes, $\epsilon = \pm 0.200$. Calculations with different amplitudes revealed behaviour similar to that depicted in figures 2–10. As an example, in figure 11 (*a*, *b*) we present two advanced stages in the evolution of an oblate perturbation of initial amplitude $\epsilon = -0.300$, for $\Gamma = 0$, and 0.050. For oblate perturbations, decreasing ϵ reduces the size of the ejected tail as well as the amount of entrained fluid, and reduces the diameter of the developing drop ring. Furthermore, decreasing ϵ reduces the magnitude of surface tension necessary for the perturbation to decay, and the drop to regain its spherical shape.

4. Closing remarks

We performed a parametric study of the nonlinear instability of a moving viscous drop. Our calculations revealed three basic mechanisms in the drop evolution: ejection of a tail, reduction of the drop into a nearly steady ring, and filamentation. Entrainment of ambient fluid was observed for both oblate and prolate perturbations. This is in contrast with results of linear theory, but in agreement with the observations of Kojima *et al.* (1984). Our nonlinear analysis was not able to explain all stages in the drop evolution reported by Kojima *et al.* (1984) and, in particular, the flattening of the rear of the drop for prolate perturbations, and the expansion of the developed drop ring. It appears that inertial effects are important during these stages of the motion.

Several authors have performed numerical studies of drop and cell deformations using the boundary-integral method for the specific case of fluids with equal

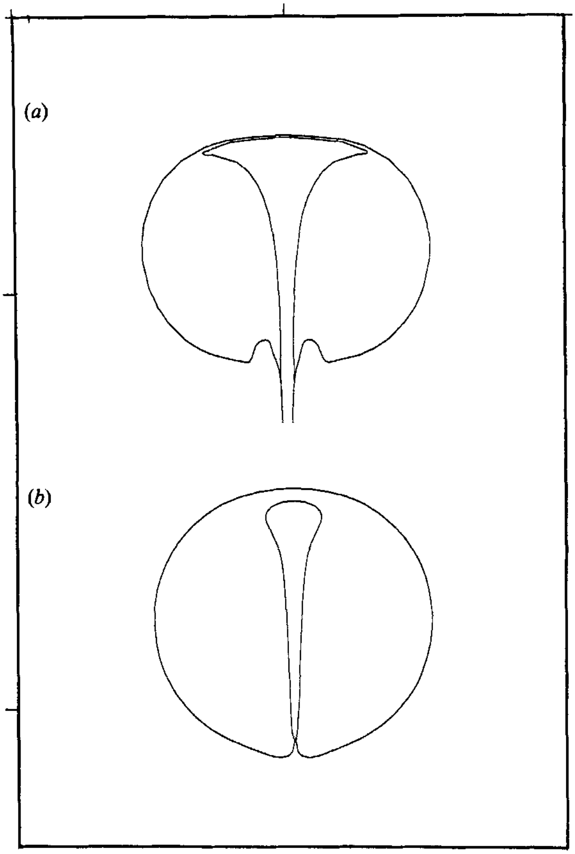

FIGURE 11. Characteristic stages in the evolution of an oblate drop with $\epsilon = -0.300$, for viscosity ratio $\lambda = 1.0$ and different magnitudes of the surface tension (a) $\Gamma = 0$, $t = 68.70$, (b) $\Gamma = 0.050$, $t = 62.00$.

viscosity, $\lambda = 1$ (Rallison 1984; Zinemanas & Nir 1988). This choice is motivated by the resulting simplifications in the numerical procedure, as discussed in §2.3. Our computations show that λ may have a significant effect on the qualitative features of the evolution, and suggest reconsideration of the problems studied by the above authors for general values of the viscosity ratio.

I would like to thank Professor Bruce Driver of the Department of Mathematics of UCSD for an enlightening conversation. Thanks are due to the office of academic computing of UCSD for providing computer time with the SDSC. Acknowledgment is made to the donors of The Petroleum Research Fund, administered by the ACS, for partial support of this research. This work was partially supported by the NSF, Grant MSM 88-20350.

Appendix A

In this appendix we show that the homogeneous integral equation (2.16*b*), where β and q are complex, may have only real eigenvalues with $|\beta| \geqslant 1$. In our proof, we trace the steps of the corresponding theory for potential flow (Bergman & Schiffer

1953, p. 172), Thus, assuming that $\boldsymbol{q}$ is a solution to (2.16*b*), we define the complex function

$$w_i(\boldsymbol{x}_0) = \frac{1}{4\pi}\int_S S_{ij}(\boldsymbol{x}_0, \boldsymbol{x})\, q_j(\boldsymbol{x})\, \mathrm{d}S(\boldsymbol{x}). \tag{A 1}$$

This represents a continuous velocity field induced by a distribution of Stokeslets. The corresponding surface stress experiences a discontinuity of magnitude $2\boldsymbol{q}$ across S. The limiting values of the surface stress on either side of S are given by

$$(\sigma_{ik}\hat{n}_k)^{\pm}(\boldsymbol{x}_0) = -(\pm)\,\mu q_i(\boldsymbol{x}_0) + \frac{\mu}{4\pi}\hat{n}_k(\boldsymbol{x}_0)\int_S^{I_{\mathrm{PV}}} T_{ijk}(\boldsymbol{x}_0, \boldsymbol{x})\, q_j(\boldsymbol{x})\, \mathrm{d}S(\boldsymbol{x}), \tag{A 2}$$

where the plus sign is for the external, and the minus sign for the internal, side of S. Combining (2.16*b*) and (A 2) we obtain

$$(\sigma_{ik}\hat{n}_k)^{\pm} = -\mu(\pm 1 - 1/\beta)\, q_i. \tag{A 3}$$

Next, we use the identities

$$2\mu\int_{V^+} e_{ik}\, e_{ik}^*\, \mathrm{d}V = -\int_{S^+} w_i^*\, \sigma_{ik}\, \hat{n}_k\, \mathrm{d}S, \tag{A 4a}$$

$$2\mu\int_{V^-} e_{ik}\, e_{ik}^*\, \mathrm{d}V = \int_{S^-} w_i^*\, \sigma_{ik}\, \hat{n}_k\, \mathrm{d}S, \tag{A 4b}$$

where $\boldsymbol{e} = \frac{1}{2}[\nabla\boldsymbol{w} + (\nabla\boldsymbol{w})^{\mathrm{T}}]$ is the rate of deformation tensor, $\boldsymbol{\sigma}$ is the stress tensor corresponding to the flow $\boldsymbol{w}$, and an asterisk indicates the complex conjugate (Ladyzhenskaya 1969, p. 53). Inserting (A 3) into (A 4*a*,*b*) we obtain

$$2\int_{V^+} e_{ik}\, e_{ik}^*\, \mathrm{d}V = -(1/\beta - 1)\int_{S^+} w_i^*\, q_i\, \mathrm{d}S, \tag{A 5a}$$

$$2\int_{V^-} e_{ik}\, e_{ik}^*\, \mathrm{d}V = (1/\beta + 1)\int_{S^-} w_i^*\, q_i\, \mathrm{d}S. \tag{A 5b}$$

The integrals on the right-hand side are identical, for $\boldsymbol{w}$ is a continuous function. Adding the above equations, and noting that the integral on the left-hand side is real and non-negative, indicates that the integral on the right-hand side is real and non-negative as well. As a consequence, β must be real. Furthermore, multiplying (A 5*a*) by (A 5*b*) side by side, we obtain $\beta^2 \geqslant 1$ which is the desired result.

Appendix B

In this appendix we give the defining expressions for the various matrices introduced in the paper.

The matrix $\boldsymbol{M}$ is defined as

$$M_{11} = \sigma(I_{10} + \hat{x}^2 I_{30}), \quad M_{12} = \sigma\hat{x}(\sigma I_{30} - \sigma_0 I_{31}), \quad M_{21} = \sigma\hat{x}(\sigma I_{31} - \sigma_0 I_{30}),$$
$$M_{22} = \sigma(I_{11} + (\sigma^2 + \sigma_0^2)\, I_{31} - \sigma\sigma_0(I_{30} + I_{32})).$$

The matrix $\boldsymbol{q}$ is defined as

$$q_{111} = -6\sigma\hat{x}^3 I_{50}, \quad q_{112} = q_{121} = -6\sigma\hat{x}^2(\sigma I_{50} - \sigma_0 I_{51}), \quad q_{211} = -6\sigma\hat{x}^2(\sigma I_{51} - \sigma_0 I_{50}),$$
$$q_{122} = -6\sigma\hat{x}(\sigma_0^2 I_{52} + \sigma^2 I_{50} - 2\sigma\sigma_0 I_{51}), \quad q_{221} = q_{212} = -6\sigma\hat{x}((\sigma^2 + \sigma_0^2)\, I_{51} -$$
$$\sigma\sigma_0(I_{50} + I_{52})), \quad q_{222} = -6\sigma(\sigma^3 I_{51} - \sigma_0^3 I_{52} - \sigma^2\sigma_0(I_{50} + 2I_{52}) + \sigma\sigma_0^2(I_{53} + 2I_{51})).$$

The matrix $\boldsymbol{p}$ is defined as

$$p_{11} = q_{211}, \quad p_{12} = q_{212}, \quad p_{21} = -6\sigma\hat{x}(\sigma^2 I_{52} + \sigma_0^2 I_{50} - 2\sigma\sigma_0 I_{51}),$$
$$p_{22} = -6\sigma(\sigma^3 I_{52} - \sigma_0^3 I_{51} - \sigma^2\sigma_0(I_{53} + 2I_{51}) + \sigma\sigma_0^2(I_{50} + 2I_{52})).$$

The matrix $\boldsymbol{h}$ is defined as

$$h_{111} = q_{111}, \quad h_{112} = q_{211}, \quad h_{121} = q_{121}, \quad h_{211} = q_{211},$$
$$h_{122} = q_{212}, \quad h_{221} = q_{221}, \quad h_{212} = p_{21}, \quad h_{222} = p_{22}.$$

In all of the above,

$$I_{mn} = \int_0^{2\pi} \frac{\cos^n \phi}{I^m} \mathrm{d}\phi = \frac{1}{[\hat{x}^2 + (\sigma+\sigma_0)^2]^{m/2}} \int_0^{\frac{1}{2}\pi} \frac{(2\cos^2\omega - 1)^n}{\Delta^m} \mathrm{d}\omega,$$

where
$$\Delta = (1 - k^2\cos^2\omega)^{\frac{1}{2}}, \quad k^2 = \frac{4\sigma\sigma_0}{\hat{x}^2 + (\sigma+\sigma_0)^2}.$$

The last integral may be expressed with the aid of standard tables in terms of complete elliptic integrals of the first and second kind (Gradshteyn & Ryshik 1980, §2.58).

REFERENCES

Baker, G. R., Meiron, D. I. & Orszag, S. A. 1982 Generalized vortex methods for free-surface flow problems. *J. Fluid Mech.* **123**, 477–501.

Batchelor, G. K. 1967 *An Introduction to Fluid Dynamics.* Cambridge University Press.

Bergman, S. & Schiffer, M. 1953 *Kernell Functions and Elliptic Differential Equations in Mathematical Physics.* Academic.

Clift, R., Grace, J. R. & Weber, M. E. 1978 *Bubbles, Drops, and Particles.* Academic.

Delves, L. M. & Mohamed, J. L. 1985 *Computational Methods for Integral Equations.* Cambridge University Press.

Gradshteyn, I. S. & Ryshik, I. M. 1980 *Table of Integrals, Series, and Products.* Academic.

Griffiths, R. W. 1986 Thermals in extremely viscous fluids, including the effects of temperature-dependent viscosity. *J. Fluid Mech.* **166**, 115–138.

Harper, J. F. 1972 The motion of bubbles and drops through liquids. *Adv. Appl. Mech.* **12**, 59–129.

Kojima, M., Hinch, E. J. & Acrivos, A. 1984 The formation and expansion of a toroidal drop moving in a viscous fluid. *Phys. Fluids* **27**, 19–32.

Korn, G. A. & Korn, T. M. 1968 *Mathematical Handbook for Scientists and Engineers.* McGraw-Hill.

Ladyzhenskaya, O. A. 1969 *The Mathematical Theory of Viscous Incompressible Flow* (2nd edn.) Gordon & Breach.

Power, H. 1987 On the Rallison and Acrivos solution for the deformation and burst of a viscous drop in an extensional flow. *J. Fluid Mech.* **185**, 547–550.

Rallison, J. M. 1981 A numerical study of the deformation and burst of a viscous drop in general shear flows. *J. Fluid Mech.* **109**, 465–482.

Rallison, J. M. 1984 The deformation of small viscous drops and bubbles in shear flows. *Ann. Rev. Fluid Mech.* **16**, 45–66.

Rallison, J. M. & Acrivos, A. 1978 A numerical study of the deformation and burst of a viscous drop in an extensional flow. *J. Fluid Mech.* **89**, 191–200.

Stone, H. A. & Leal, L. G. 1989 Relaxation and breakup of an initially extended drop in an otherwise quiescent fluid. *J. Fluid Mech.* **198**, 399–427.

Zinemanas, D. & Nir, A. 1988 On the viscous deformation of biological cells under anisotropic surface tension. *J. Fluid Mech.* **193**, 217–241.